Enhancement of Common-Mode Power Extraction Through Zero-Sequence Injection in Pulsewidth Modulation

Rongpei Zhu, *Graduate Student Member, IEEE*, Guang Yang, Hongyang Liu, Longyuan Fan, *Graduate Student Member, IEEE*, Zicheng Liu, *Senior Member, IEEE*, and Ronghai Qu, *Fellow, IEEE*

***Abstract*—In motor drive system fed by voltage source inverter, common-mode voltage (CMV) is commonly present because of pulsewidth modulation (PWM) techniques. It is proved to be feasible in research to collect energy from CMV and provide a dc power source for low-power sensors such as encoders. This approach can replace auxiliary power supply, thus, simplifying system wiring design. However, the practicality of this approach will be largely constrained by the maximum power available from CMV, as it directly affects the stable operation of sensors. This article aims to explore methods to improve the power capacity with low cost. A common-mode (CM) power transfer model is constructed to clarify the factors influencing CM power extraction and analyze possible methods for increasing power capacity. Then, from the perspective of power source, the characteristics of CMV are analyzed including its frequency composition and rms value. Further exploration is conducted to analyze the influence of zero-sequence injection during modulation on the characteristics of CMV. At last, a discontinuous PWM method DPWM3 is identified as the most effective PWM method to significantly enhance power capacity. Experimental results validate the accuracy of quantitative analysis and effectiveness of the proposed method.**

***Index Terms*—Common-mode voltage (CMV), inverter, power capacity, pulsewidth modulation, zero-sequence injection.**

I. Introduction

With the development of power electronic technology, the capacity and switching frequency of power semiconductors continue to increase. Thus, voltage source inverters (VSIs) and pulsewidth modulation (PWM) technology are widely applied in the field of motor control to flexibly regulate the output voltage. However, due to the fact that the output voltage of VSI is essentially a discrete pulse sequence, common-mode voltage (CMV) is generated at the neutral point of the motor stator winding. High-frequency and high-amplitude CMV can lead to severe electromagnetic interference (EMI) issues, causing interference with sensitive equipment [1]. Additionally, CMV generates common-mode (CM) current through parasitic parameters in the system, exacerbating insulation aging of motor windings and electricity loss of bearings [2], [3].

Efforts have long been made to suppress CMV to mitigate its harmful effects. Currently, CMV suppression methods are mainly divided into passive and active methods. Passive methods mainly involve reducing common-mode EMI by adding hardware circuits [4], [5], [6], [7], while active methods mainly involve changing PWM strategies to reduce dv/dt of CMV. Compared to passive methods, active methods have advantages of low cost and strong adaptivity [8]. Active CMV suppression methods can mainly be achieved by avoiding the use of zero vectors, such as active zero state PWM [9] and near state PWM [10], or by adopting carrier phase-shifted PWM (PS-PWM) [11]. However, in general, it is difficult to completely eliminate CMV, especially for odd-phase motors.

Fan et al. [12] proposed a novel approach, suggesting the collection of energy from CMV rather than its elimination, to supply power to motor sensors such as encoders. Encoders often require additional low dc voltage power, resulting in extra cables for the motor control system. For industrial robots, the additional power line will reduce the flexibility and increase the safety risk during operation. In the drilling industry, because of the massive losses in the long cable line of well submersible electric motor and harsh downhole environment, it is not realistic to down an extra cable of the encoder to the bottom of the well. There are some self-powered encoders currently but they usually rely on the rotational shaft of the motor [13], [14], [15]. When the motor is stationary or rotating at low speed, inadequate power supply to the encoder may result in the loss of rotor position information.

Harvesting power from other parts of the motor system can also be used to design an integrated auxiliary power supply for sensors, but each scheme has its own drawbacks considering the mentioned special application scenarios. Harvesting power from input dc voltage (through dc–dc converter) can provide a stable output but long cables are unavoidable when supplying

Received 3 March 2025; revised 9 June 2025 and 9 August 2025; accepted 12 September 2025. Date of publication 17 September 2025; date of current version 13 November 2025. This work was supported by the National Natural Science Foundation of China (NSFC) under Grant 52077088. Recommended for publication by Associate Editor D.-C. Lee. *(Corresponding author: Zicheng Liu.)*

Rongpei Zhu, Longyuan Fan, Zicheng Liu, and Ronghai Qu are with the State Key Laboratory of Advanced Electromagnetic Engineering and Technology, School of Electrical and Electronic Engineering, Huazhong University of Science and Technology, Wuhan 430074, China (e-mail: m202372475@hust.edu.cn; flyin@hust.edu.cn; liuzc@hust.edu.cn; ronghaiqu@hust.edu.cn).

Guang Yang and Hongyang Liu are with AVIC Xi'an Flight Automatic Control Research Institute, Xi'an 710065, China (e-mail: yangg073@avic.com; liuhy076@avic.com).

Color versions of one or more figures in this article are available at https://doi.org/10.1109/TPEL.2025.3611381.

Digital Object Identifier 10.1109/TPEL.2025.3611381

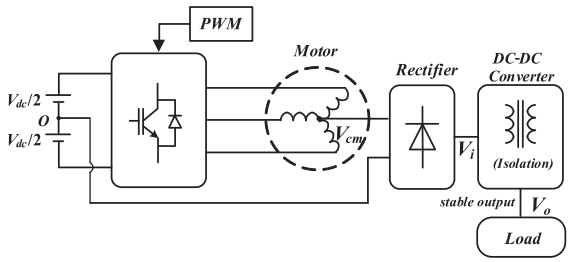

Fig. 1. CM power extraction scheme of three phase topology.

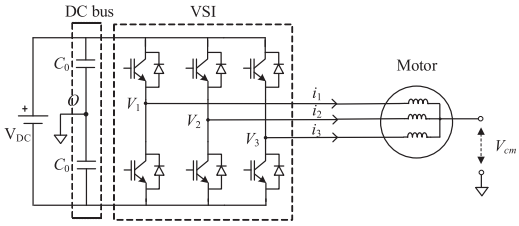

Fig. 2. Typical three-phase VSI driving system.

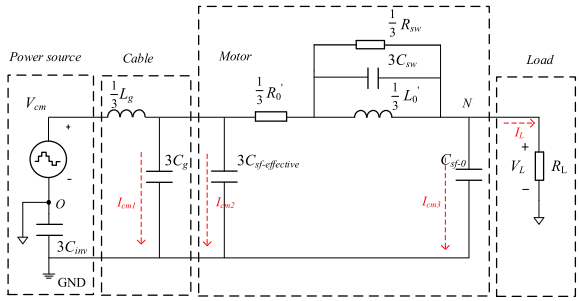

Fig. 3. Universal model for equivalent CM load circuit.

power to sensors located near the motor. Harvesting power from the motor's input voltage (through rectifier and dc–dc converter) relies on the differential-mode voltage component of motor control. When the motor is stationary, since the differential-mode voltage is zero, this scheme cannot work properly. Harvesting power from CMV (through rectifier and dc–dc converter) could avoid these two issues. Since CMV persists even when the motor is stationary, it can provide a stable power source for encoders. Furthermore, CMV exists at the neutral point of the motor, which is internal to the motor, facilitating the integrated design of auxiliary power circuit nearby the motor.

However, a concern with this approach is whether the power provided by CMV throughout the entire speed range of motor operation can reliably supply power to the encoder. Fan et al. [16] employed sinusoidal PWM (SPWM) to drive the motor. When the modulation index is high, the CM power extraction is significantly reduced. To enhance power capacity, Fan et al. [16] proposed the use of series-resonant capacitors. However, this method requires additional hardware circuits. Additionally, when the switching frequency of VSI changes, capacitors need to be replaced to rematch the resonance point, resulting in limited flexibility. Park et al. [17] proposed the use of CMV to drive a single-phase, low-power ac motor, which reduces the component costs in multimotor systems. However, the adoption of a modulation method with an offset voltage reduces the dc voltage utilization and results in significant distortion of the phase current.

This article aims to enhance the power supply capability of CMV while not significantly affecting the normal operation of the motor, thereby improving the universality of CM power extraction scheme for VSI systems. In Section II, a model of CM power transfer is established. Factors influencing power supply capability of CMV are analyzed based on circuit power transmission theory. In Section III, from the perspective of excitation sources, the frequency composition and rms value of CMV under different PWM strategies are analyzed. Based on zero-sequence injection, a modulation method aimed at enhancing the power supply capability of CMV is explored and proposed. In Section IV, experiments are carried out on a 2.2 kW three-phase induction motor, validating the correctness of the quantitative theory and power enhancement methods. Finally, Section V concludes this article.

II. Modeling and Analysis of CM Power Circuit

Taking the three-phase motor drive system topology as an example, the CM power extraction scheme [12] is illustrated in Fig. 1. Under PWM techniques, VSI generates pulse output voltage to the motor, resulting in the generation of CMV at the neutral point of the motor, which can be calculated by

$$V_{\text{cm}} = \frac{V_1 + V_2 + V_3}{3}. \tag{1}$$

The CMV then undergoes rectifier and dc–dc converter to provide stable dc voltage for load such as encoders. The dc–dc converter with isolation functionality ensures that the high-power side of the motor and the low-power side of the sensors would not interfere with each other. To ascertain the factors influencing CM power extraction, it is necessary to model the CM power extraction circuit and analyze the influence of circuit parameters.

A. Model of Common-Mode Power Circuit

A typical inverter control system for a three-phase motor is depicted in the Fig. 2. Define the CMV as the voltage from the motor neutral point to the midpoint O of the dc bus. Modeling of the CM power extraction circuit is mainly based on the high-frequency impedance models of the inverter and motor stator due to the presence of high-frequency components in CMV. Fan et al. [16] proposed a generalized CM power extraction circuit model, as shown in Fig. 3.

Where C_{inv} is the inverter impedance of each phase to ground. L_g is the parasitic inductance of power cables; C_g is the capacitance between cables and ground. It should be noted that when the cable length reaches 500–4000 m, the cable can contribute a non-negligible impedance. Additionally, overvoltage oscillation will occur at the motor terminal, thus, influence the waveform of CMV [18]. In such cases, priority should be given to mitigating this effect to ensure the normal operation of the motor [19]. $C_{sf\text{-effective}}$ is the effective stator-to-frame capacitance of the first few turns per phase while $C_{sf\text{-}0}$ is the stator-to-frame capacitance in Y neutral [20]; R_0 is the stator resistance; L_0' is the

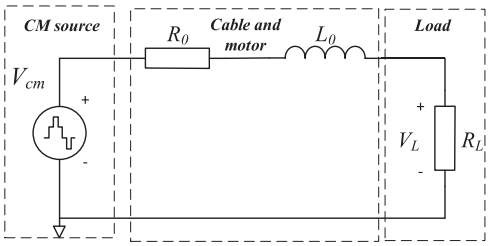

Fig. 4. Simplified model for equivalent CM load circuit.

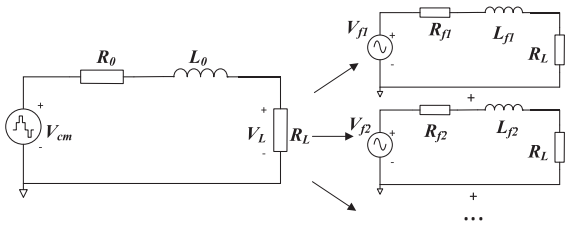

Fig. 5. Analysis of CM power extraction based on Fourier decomposition.

stator leakage inductance; C_{sw} is the stator turn-to-turn winding capacitance; R_{sw} is stator turn-to-turn damping resistance in winding. R_L is the equivalent load. O represents the midpoint of the dc bus, while GND denotes ground.

The circuit comprises two branches: one is the noise circuit from power source to GND, the other is the load circuit to the midpoint O of dc bus. The CM power extraction circuit corresponds to the latter.

In fact, it is quite challenging to measure all the parameters and calculate the CM power using this complex CM power extraction circuit. Typically, the parallel parasitic capacitance in the circuit is in the picofarad range [16], and the circuit switching frequency ranges from several kHz to tens of kHz. The impedance of the parallel capacitor is much bigger than the impedance of the motor stator inductance, so we can regard it as open-circuit. Therefore, we can simplify the circuit model using the Thévenin theorem, as shown in Fig. 4. The circuit predominantly exhibits inductive behavior.

Utilizing this model, it becomes easy to calculate the load power. Initially, by treating $V_{\rm cm}$ as a single-frequency ac power source, the total circuit impedance and load power can be calculated from the diagram

$$\dot{Z} = j\omega L_0 + R_0 + R_L = jX_0 + R_0 + R_L \tag{2}$$

$$\dot{I}_L = \frac{\dot{V}_{\rm cm}}{\dot{Z}} \tag{3}$$

$$|\dot{I}_L| = \frac{\left|\dot{V}_{\rm cm}\right|}{\sqrt{(R_0 + R_L)^2 + X_0^2}} \tag{4}$$

$$P_L = |\dot{I}_L|^2 \cdot R_L = \frac{\left|\dot{V}_{\rm cm}\right|^2}{\frac{R_0^2+X_0^2}{R_L} + R_L + 2R_0}. \tag{5}$$

For (5), when $R_L^2 = R_0^2 + X_0^2$, $P_L$reaches its maximum value, which is

$$P_{L\max} = \frac{\left|\dot{V}_{\rm cm}\right|^2}{2\cdot\left(R_0+\sqrt{R_0^2+X_0^2}\right)}. \tag{6}$$

$R_L^2 = R_0^2 + X_0^2$, that is

$$R_L = \sqrt{R_0^2 + X_0^2} = Z_0. \tag{7}$$

Equation (7) implies that when the load R_L equals the equivalent impedance of the circuit Z_0, the load power can reach its maximum value.

B. Power Analysis of CMV Multifrequency Components

CMV is actually composed of multiple frequencies. Therefore, the analysis of CM power extraction should be based on Fourier decomposition. The CM power extraction circuit is decomposed into several circuits based on the principle of single frequency. These circuits have different ac voltage source (different frequency and amplitude) and circuit impedances. The load power is then calculated for each single frequency circuit and summed up to obtain the total power, as illustrated in Fig. 5.

The maximum power obtainable by the circuit is dependent on the rms value of the CMV and the circuit impedance. The magnitude of the circuit reactance X_0 and resistance R_0 is not only influenced by factors such as the winding design of the motor stator but also closely related to frequency, as evident from $X_0 = 2\pi f L_0$. Additionally, high-frequency current will induce significant skin effect, resulting in noticeable frequency characteristics of R_0. Therefore, when performing frequency decomposition of the CM power extraction circuit, it is essential to clarify the relationship between the impedance of the circuit and frequency.

Fig. 6 shows the frequency response of the circuit's equivalent resistance, inductance, and its reactance on the studied induction motor. Here, we mainly consider two specific frequency ranges. One is the fundamental frequency range, where the fundamental current is used to drive the motor rotation, typically ranging from tens to hundreds of Hz. The other is the switching frequency range, corresponding to the harmonics generated when the power electronic circuit switches, typically around several kHz to tens of kHz. It can be observed that within these two frequency ranges, the circuit's resistance R_0 significantly increases due to the skin effect of high-frequency current, while the reactance X_0 also notably increases as it is directly proportional to the frequency.

Further discussion is conducted on the difference in CM power extraction circuit between the fundamental frequency range and the switching frequency range. Assuming a fundamental frequency f_0 of 50 Hz and a switching frequency f_s of 10 kHz, the power provided by the circuits in these two frequency ranges is as follows:

$$P_L' = P_{fs} + P_{f0} = \frac{{V_{fs}}^2}{\frac{R_{fs}^2+X_{fs}^2}{R_L} + R_L + 2R_{fs}} + \frac{{V_{f0}}^2}{\frac{R_{f0}^2+X_{f0}^2}{R_L} + R_L + 2R_{f0}}. \tag{8}$$

At the switching frequency of 10 kHz, according to the impedance-frequency curve, the circuit resistance is 70 Ω, and

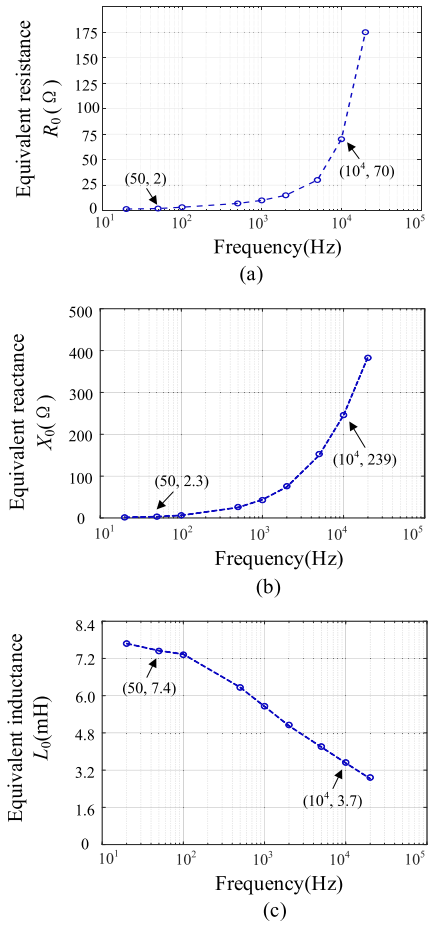

Fig. 6. Frequency response of (a) equivalent resistance, (b) reactance, and (c) inductance.

the inductance is 3.7 mH. Thus,

$$X_{fs} = 2\pi f_s L_{fs} = 2\pi \times 10^4 \times 3.7 \times 10^{-3}\Omega = 239\Omega$$

$$Z_{fs} = \sqrt{X_{fs}^2 + R_{fs}^2} = \sqrt{239^2 + 70^2}\Omega = 249\Omega.$$

At the fundamental frequency of 50 Hz, the circuit resistance is approximately 2 Ω, and the inductance is 7.4 mH. Thus,

$$X_{f0} = 2\pi f_0 L_{f0} = 2\pi \times 50 \times 7.4 \times 10^{-3}\Omega = 2.3\Omega$$

$$Z_{f0} = \sqrt{X_{f0}^2 + R_{f0}^2} = \sqrt{2.3^2 + 2^2}\Omega = 3.07\Omega.$$

Comparing with (6) and substituting the above values, it can be seen that when the voltage amplitudes of these two frequency circuits are equal, their denominators differ by more than sixty times. Consequently, the maximum power that the two circuits can provide differs by more than sixty times.

In Section II-A, only a single frequency power source is considered. According to (7), each circuit has a unique extreme (maximum) power operating point, which occurs when the load resistance matches the circuit's impedance. Based on this property, the operating point can be determined when measuring the maximum power. For example, if the power obtained with a load resistance of 100 Ω is greater than that obtained with a load resistance of 50 Ω, then the maximum load operating point must be greater than 100 Ω.

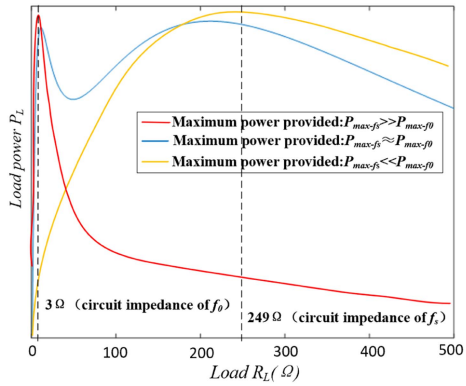

Fig. 7. Three typical Power-Load curves when relationship between the maximum power provided by fundamental frequency and switching frequency circuits changes.

However, this situation changes when considering more than one circuit. In (8), substituting the parameters in the denominators with the previously calculated results and adjusting the voltage amplitude in the numerator to change the relationship between the maximum power of the two circuits, three different power-load (P_L-R_L) curves can be obtained, as shown in Fig. 7.

According to the principle of load and circuit impedance matching, the fundamental frequency circuit achieves maximum power when the load is 3 Ω, while the switching frequency circuit achieves maximum power when the load is 249 Ω. When one circuit provides significantly more power than the other, the P_L-R_L curve has only one extreme value, which is near the load matching point of the circuit providing the higher power. When the difference in power provided by the two circuits is not significant, the P_L-R_L curve has two extreme values, each near the load matching point of each circuit. Further comparison is needed to determine, which extreme value is the maximum point. This will also be instructive when measuring the load power capacity in experiment in Section IV.

C. Factors That Affect Common-Mode Power Extraction

Analyze CM power extraction from the perspectives of source, path, and load. Generally, the load is immutable, depending on how much energy the encoder and other sensors need to extract from CMV. Therefore, the factors influencing CM power extraction are mainly analyzed from the perspectives of source and path.

According to (6), the maximum power that a certain frequency component of CMV can provide is directly proportional to the square of its voltage amplitude, and is inversely proportional to the impedance of circuit. Through the discussion in Section II-B, it can be observed that the magnitude of the circuit's impedance differs significantly between low and high frequency ranges. Thus, the potential of maximum power that can be provided in low-frequency range is much greater than that in high-frequency range. Additionally, the source and path are coupled because the frequency components of CMV determine, which frequency ranges of the circuit's impedance should be considered. To

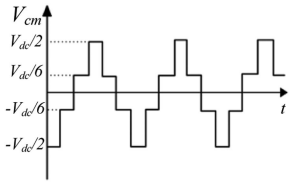

Fig. 8. CMV waveform under SPWM.

increase CM power, efforts should be made to increase the low-frequency components of CMV. Therefore, finding a suitable source is the key to improving CM power extraction.

III. Influence of Zero-Sequence Injection on the Characteristics of CMV

Under different PWM methods, the discrete pulses output by VSI are distinct. Therefore, according to (1), the characteristics of CMV are primarily determined by different PWM methods. This section mainly discusses the characteristics of CMV generated by various PWM methods.

A. Effect of Zero-Sequence Injection on the Frequency Components of CMV

SPWM is the most typical method for approximating sine waves through carrier wave comparison. Fig. 8 illustrates the CMV waveform under SPWM, where there are four voltage levels, with a maximum amplitude of $V_{\rm dc}/2$. Harmonic analysis of the phase output pulse voltage generated by SPWM can be performed using double Fourier decomposition, leading to the expression of CMV.

The universal expression for phase A voltage [21] is

$$\begin{aligned} V_{ao} = &\sum_{n=1}^{\infty}\left[A_{0n}\cos n\left(\omega_0 t\right) + B_{0n}\sin n\left(\omega_0 t\right)\right] \\ &+ \sum_{m=1}^{\infty}\sum_{n=-\infty}^{\infty}\left[A_{mn}\cos\left(m\omega_s t + n\omega_0 t\right)\right. \\ &\left. + B_{mn}\sin\left(m\omega_s t + n\omega_0 t\right)\right] \end{aligned} \tag{9}$$

where m is the index for the carrier wave, and n is the index for the modulation wave. The first sum represents the fundamental component and its baseband harmonics, while the second sum represents the harmonic components of the carrier wave and its sideband harmonics. The expressions for phase B and C only require phase shifting from phase A.

Based on the definition of CMV, the expression of CMV under SPWM can be obtained as follows:

$$\begin{aligned} V_{\rm cm} = &\frac{1}{3}\sum_{m=1}^{\infty}\sum_{n=-\infty}^{\infty} A_{mn}\cdot\left(1+2\cos\frac{2n\pi}{3}\right) \\ &\cdot\cos\left(m\omega_s t + n\omega_0 t\right) \end{aligned} \tag{10}$$

$$A_{mn} = \frac{2V_{\rm dc}}{m\pi}J_n\left(\frac{\pi}{2}mM\right)\sin\left[\frac{\pi}{2}\left(m+n\right)\right] \tag{11}$$

where M is the modulation index, defined as the ratio of the amplitude of the output fundamental frequency voltage to the dc bus voltage. J_n is the Bessel function. As the modulation index M changes, the characteristics of CMV also change. The maximum modulation index M for SPWM is 1. Within the overmodulation range ($M > 1$), the high-frequency harmonic characteristics of the output waveform deteriorate, which is not conducive to filtering. Therefore, it is advisable to avoid the inverter operating within the overmodulation range as much as possible. Thus, we mainly consider the CMV characteristics within the linear region.

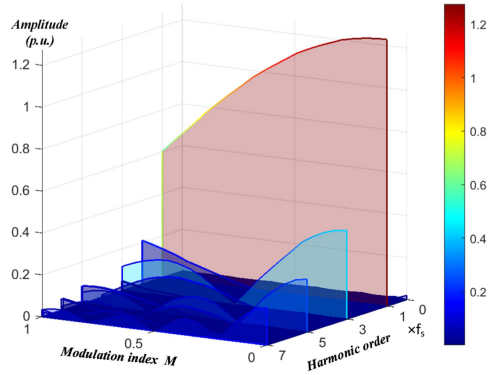

Fig. 9. Harmonic distribution of CMV under SPWM as a function of modulation index.

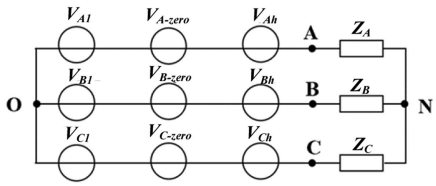

Fig. 10. Decomposition of output voltage in three-phase topology.

Fig. 9 depicts a three-dimensional graph illustrating the harmonic distribution of CMV under SPWM while modulation index varies. In this graph, the Z-axis is normalized to the half amplitude of dc bus voltage.

From Fig. 9, it can be observed that CMV under SPWM does not contain fundamental frequency component. Instead, its frequency components are mainly distributed around the switching frequency and its harmonics, which is consistent with the conclusion from (10). Furthermore, within the entire linear modulation region, the amplitude of the switching frequency component keeps the largest. Therefore, in analysis process, it can be considered that the primary excitation is the switching frequency component.

SPWM suffers from the issue of low utilization of dc bus voltage. To improve voltage utilization, some zero-sequence components can be injected to the modulation wave. For example, in case of three-phase topology, the third harmonic is the most typical zero-sequence component. During analysis, the generated output voltage can be decomposed into fundamental component (V_1), zero-sequence components ($V_{\rm zero}$), and high-frequency components (V_h), as shown in Fig. 10. In a three-phase topology with a star connection without a neutral wire, due to the Kirchhoff's current law at the neutral point N, zero-sequence current cannot flow. Therefore, CMV at N must

contain zero-sequence components. In other words, injecting zero-sequence components into the modulation wave does not affect the sinusoidal performance of the output waveform, but it can introduce zero-sequence components into the CMV.

Injection of zero-sequence components complicates the mathematical harmonic analysis expression of phase voltage considerably. However, to improve power extraction, we only need to focus on the third harmonic and other low-frequency zero-sequence injection components. When injecting zero-sequence components into the modulation wave, the calculation of coefficients A_{mn} and B_{mn} in double Fourier decomposition involves changes in the integration limits

$$A_{mn}+jB_{mn}=\frac{1}{2\pi^2}\times\int_{-\pi}^{\pi}\int_{-\frac{\pi}{2}(1+M\cos y+M_{3k}\cos 3ky)}^{\frac{\pi}{2}(1+M\cos y+M_{3k}\cos 3ky)}V_{\mathrm{dc}}e^{j(mx+ny)}dxdy \quad (12)$$

where $k=0,\ 1,\ 2\ldots$ represents the injected zero-sequence components in the modulation wave. When $m=0$ and $n>0$, (12) represents the amplitude of modulation-wave-related frequency components generated in phase voltage, which is the low-frequency component of the CMV that we are interested in

$$A_{0n}+jB_{0n}=\frac{V_{\mathrm{dc}}}{2\pi}\int_{-\pi}^{\pi}\left\{e^{jny}+\frac{M}{2}\left[e^{j(n+1)y}+e^{j(n-1)y}\right]+\frac{M_{3k}}{2}\left[e^{j(n+3k)y}+e^{j(n-3k)y}\right]\right\}dy \quad (13)$$

when n = 1, $A_{01}+jB_{01}=\frac{V_{\mathrm{dc}}}{2}M$; when n = 3 k, $A_{03k}+jB_{03k}=\frac{V_{\mathrm{dc}}}{2}M_{3k}$; When n equals other values, $A_{0n}+jB_{0n}=0$.

Therefore, when there is zero-sequence component injection, the expression for phase A output voltage can be written as

$$V_{ao}=\frac{V_{\mathrm{dc}}}{2}M\cos\omega_0 t+\frac{V_{\mathrm{dc}}}{2}M_{3k}\cos(3k\omega_0 t)+\sum_{m=1}^{\infty}\sum_{n=-\infty}^{\infty}\left[A_{mn}\cos(m\omega_s t+n\omega_0 t)+B_{mn}\sin(m\omega_s t+n\omega_0 t)\right]. \quad (14)$$

The expression for CMV can be written as

$$V_{\mathrm{cm}}=\frac{V_{\mathrm{dc}}}{2}M_{3k}\cos(3k\omega_0 t)+\frac{1}{3}\sum_{m=1}^{\infty}\sum_{n=-\infty}^{\infty}A_{mn}\cdot\left(1+2\cos\frac{2n\pi}{3}\right)\cdot\cos(m\omega_s t+n\omega_0 t). \quad (15)$$

Expression (15) indicates that the amplitude of low-frequency component generated in CMV is directly proportional to the amount of corresponding zero-sequence injection in modulation wave. THISPWM injects the third harmonic of 1/6 amplitude of fundamental modulation wave so that the voltage utilization can be maximized, i.e., the maximum modulation index reaches approximately 1.15 [22]. Fig. 11 shows the harmonic distribution of CMV under THISPWM as a function of modulation index.

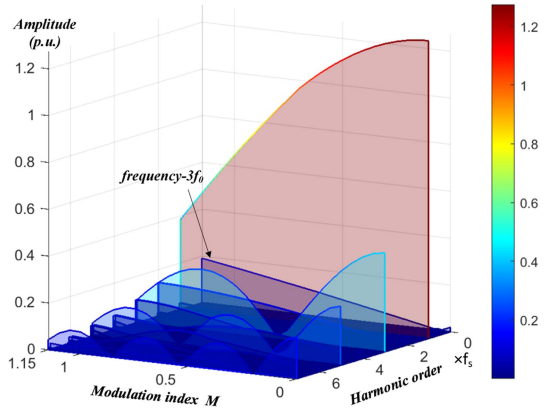

Fig. 11. Harmonic distribution of CMV under THISPWM as a function of modulation index.

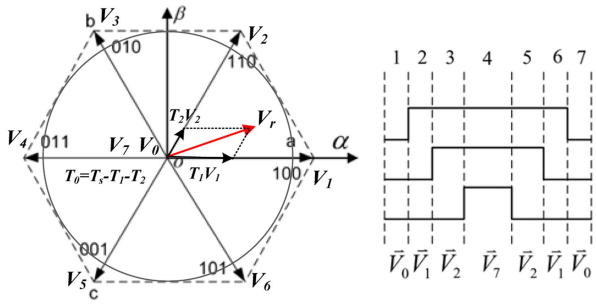

Fig. 12. Space vector modulation and typical SVPWM.

As analyzed, CMV under THISPWM contains component at triple fundamental frequency. As modulation index increases, the amplitude of the injected third harmonic in modulation wave increases, leading to a continuous increase of the amplitude of the third harmonic component in CMV. When $M=1.15$, the amplitude of this component reaches approximately 50% of the switching frequency component.

B. Effect of Zero-Sequence Injection on RMS Valve of CMV

Although zero-sequence injection can effectively increase the amplitude of low-frequency components in CMV, CMV is composed of multiple frequency components and other components can also contribute to CM power extraction. Therefore, it is necessary to discuss whether zero-sequence injection affects the total rms value of CMV. In other words, if increasing the amplitude of low-frequency components is achieved at the expense of significantly reducing the total rms value of CMV, which may not be beneficial for CM power extraction either.

Describing the rms value of CMV from space vector modulation (SVM, as shown in Fig. 12) perspective is relatively straightforward because the voltage level of CMV corresponds to the selection of space vector one-to-one. PWM methods that employ the same carrier wave in three phases use the nearest two-vector principle (NTV), which synthesizes the reference voltage from the adjacent two effective vectors in sector where the reference voltage vector lies, and balances time with the zero vector. Since the reference voltage vector is the same,

the selection and action time of effective space vectors are the same. The only difference lies in the selection of two zero vectors 000(V_0) and 111(V_7) among different PWM modulation methods. Although the selection of zero vectors may vary, the absolute values of CMV corresponding to vector V_0 and V_7 are the same, as $V_{\rm dc}/2$. According to the definition of rms value, PWM modulation methods using the NTV principle have the same rms value. It means that zero-sequence injection would not affect the rms value of CMV. Under the condition of the same total rms value, a higher amplitude of low-frequency components means a higher proportion in CMV, which is beneficial to improve CM power extraction.

SPWM can be regarded as a special case with zero-sequence injection amount of 0. The analysis of rms value of CMV under SPWM modulation can be extended to other PWM methods based on the NTV principle, where the rms value of CMV decreases as modulation index increases [16]. This phenomenon can also be explained from a space vector perspective: as modulation index increases, the magnitude of reference voltage vector Vr grows, the effective vectors' action time increases under volt-second balance principle, while the time allocated to zero vector decreases. Since the zero vector has the maximum CMV amplitude, total rms value of CMV decreases. This implies that increasing the modulation index will be disadvantageous for CM power extraction. When the motor enters the overmodulation region, the dwelling time of the zero vectors is further shortened. Upon reaching the limit —six-step mode, the zero vectors are completely removed and CMV only has two levels. At this point, the rms value of CMV reaches minimum. The principle to extract power from CMV is still available but its CM power capacity becomes limited. Therefore, from the perspective of ensuring the stability of CM power extraction, it is advisable to avoid entering the overmodulation region.

NTV principle retains the occurrence of zero vectors, thus ensuring the maximum rms value of CMV. For PWM methods that do not use the NTV principle, such as reduced CMV strategy PS-SPWM, which avoids the use of zero vectors, the small rms value of CMV similarly hinders CM power extraction.

C. Exploration of Zero-Sequence Injection to Introduce High-Amplitude Low-Frequency Components Into CMV

Based on previous analysis, injecting a higher-amplitude zero-sequence component into modulation waveform results in a higher content of low-frequency components in CMV, which is advantageous for increasing CM power extraction. However, injecting excessively high-amplitude zero-sequence components may reduce the utilization of dc voltage, so it is necessary to inject high-amplitude zero-sequence components in a rational manner.

In SVM, as long as the length of the synthesized reference voltage vector does not exceed the inscribed circle of the spatial vector hexagon, the maximum modulation index can be maintained at around 1.15. According to research, carrier-based modulation and SVM can be partially transformed into each other. The expression for the zero-sequence component injected when SVM is equivalent to carrier-based modulation is given as [23]

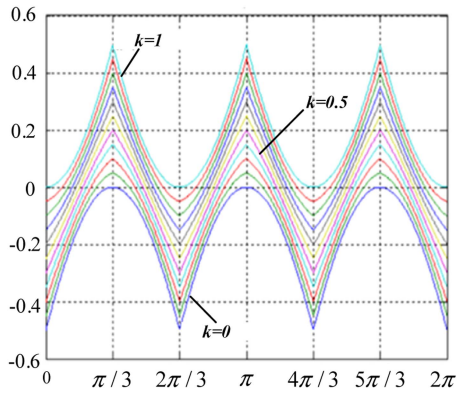

Fig. 13. Waveform of zero-sequence injection when $M = 1$ and k varies from 0 to 1.

$$e = k\,(1 - v_{\max}) + (1 - k)\,(-1 - v_{\min}) \tag{16}$$

where k represents the proportion of the zero-vector action time allocated to V_7, with $0 \le k \le 1$; $v_{\max}$ denotes the maximum value among three-phase voltages, and $v_{\min}$ represents the minimum value. This implies that zero-sequence injection can alter the distribution pattern of zero vectors, thereby changing the frequency composition of CMV.

Within one fundamental period, when the modulation index M is 1 and k changes from 0 to 1, the waveform of the zero-sequence injection is shown in Fig. 13. It can be seen that the zero-sequence injection has a high amplitude at $k = 0$ (DPWMMIN) or $k = 1$ (DPWMMAX). However, due to its asymmetry in positive and negative half-cycles, it contains a high dc component in addition to third harmonic component in CMV. Based on Section II-B, theoretically dc component has the best effect on CM power enhancement since inductance is short to dc and there is no skin effect on resistance. However, dc component will charge the dc bus capacitor, causing a potential voltage shift at midpoint O. Dc component not only does not supply power to the load, but also deteriorate the differential-mode characteristics of VSI output. When $k = 0.5$, corresponding to SVPWM, the zero-sequence injection is symmetrical in positive and negative half-cycles, without a dc component. But due to its low amplitude, the effect of increasing CM power is limited.

However, k does not necessarily need to remain constant within one fundamental period; it can be changed according to the electrical angle. From the perspective of increasing CM power supply, it is best to switch between $k = 0$ and $k = 1$ because they correspond to high-amplitude zero-sequence injection. When switching, the following rules need to be followed.

1) The switching period is 120°. 120° corresponds to triple fundamental frequency, which is the lowest-frequency zero-sequence component except for dc. It is most conducive to reducing the impedance of CM power extraction circuit.
2) Each state lasts for 60° to ensure symmetry in positive and negative half-cycles, without producing a dc component in CMV.

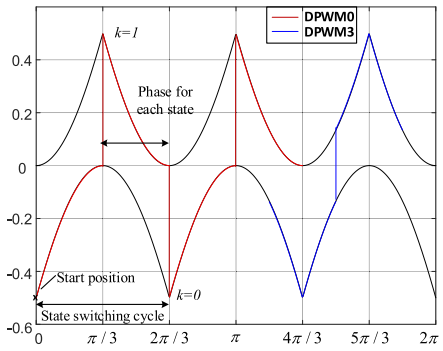

Fig. 14. Principle of $k = 0$ and $k = 1$ state switching.

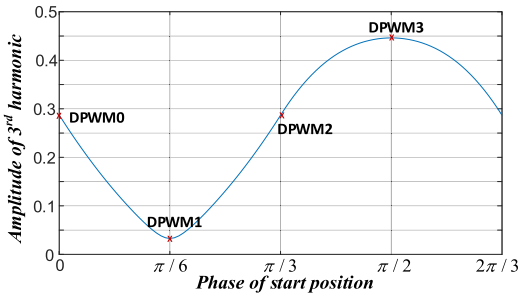

Fig. 15. Amplitude of the third harmonic in zero-sequence injection when phase of start position varies.

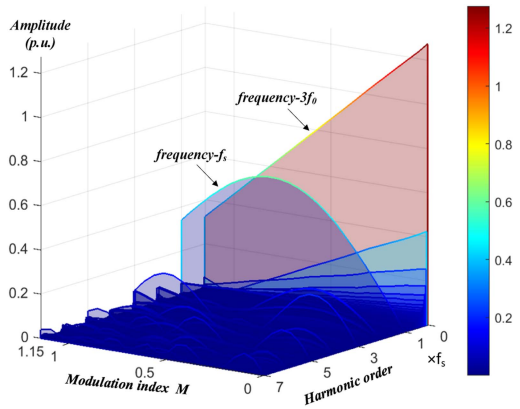

Fig. 16. Harmonics distribution of CMV under DPWM3 as a function of modulation index.

According to the two principles, within 0–120° period $k = 0$ and $k = 1$ need to be selected within a 60° interval each. But the starting position of each interval can be anywhere within 0–120°, as shown in Fig. 14. Fig. 15 shows when the starting position changes from 0 – 120° how the amplitude of the third harmonic in zero-sequence injection varies. When the starting angle of $k = 0$ is chosen as 90°, the zero-sequence waveform has the maximum amplitude of the third harmonic. This selection corresponds to DPWM3 and the waveform can be seen in Fig. 14.

The harmonics distribution of CMV under DPWM3 is shown in Fig. 16. It can be observed that the amplitude of the third harmonic component in CMV is relatively high across the entire linear modulation region, even at the maximum modulation index of $M = 1.15$, it remains almost equivalent to the switching frequency component. Compared to THISPWM, the amplitude increases by approximately 90%.

For multilevel inverter topologies, a double Fourier analysis of CMV can also be performed. The amplitude of low-frequency component generated in CMV is also directly proportional to the amount of corresponding zero-sequence injection in modulation wave. Therefore, the proposed method can also be applied to multilevel topologies. However, different multilevel topologies operate in distinct ways, and zero-sequence injection may produce other effects. For instance, in NPC topologies, zero-sequence injection can affect the neutral-point potential balance while it will not produce a significant impact in FC topologies.

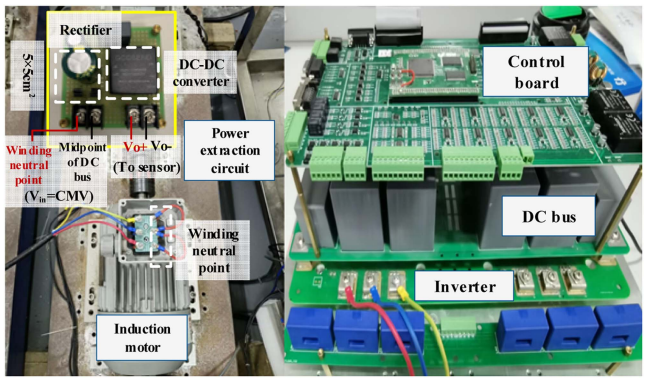

Fig. 17. Experimental setup.

IV. Experimental Results

CM power with different PWM methods is measured through experiments to validate the effectiveness of theoretical analysis. The experimental setup is shown in Fig. 17, and the experimental parameters are listed in Table I.

CMV contains harmonics at the switching frequency. Therefore, when designing the rectifier, diodes with a short reverse recovery time should be selected. Such diodes are suitable for high-frequency applications and can reduce switching losses. For the dc–dc converter, we have chosen a commercially mature integrated module. First, the dc–dc converter should possess electrical isolation between high and low voltage circuits to ensure safety. Second, since CMV varies with the motor's operating conditions, the input voltage of the dc–dc converter is unstable. Based on the Fourier decomposition results of CMV and considering a safety margin, the maximum value of the dc voltage input range can be set at 0.6 to 0.7 times the dc bus voltage. Finally, the output voltage and power of the dc–dc converter depend on the sensors.

A. CM Power Capacity Under SPWM, THISPWM, and SVPWM

When measuring CM power capacity, to facilitate comparison with the theoretical model, the CM power extraction circuit

TABLE I
EXPERIMENTAL PARAMETERS

Motor and Inverter Parameters		
Motor rated power	P_N	2.2 kW
Motor rated frequency	f_N	50 Hz
Motor rated voltage	V_N	380 V
Motor pole pair	P	1
Switching frequency	f_s	10 kHz
Dc source voltage	V_{dc}	120 V
Dc bus capacitance	C_0	4000 μF
Parameters for Case Study		
Input voltage of dc–dc converter	V_i	18 V–75 V
Output voltage of dc–dc converter	V_o	5 V
Output power of dc–dc converter	P_{out}	5 W Max

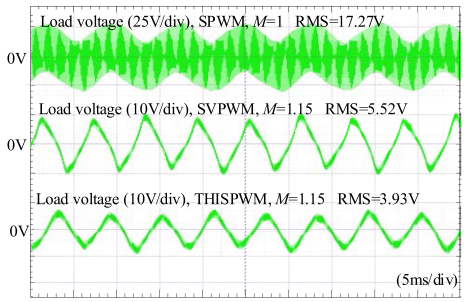

Fig. 18. Load voltage waveforms when CM power reaches maximum at a certain modulation index. The corresponding condition. (a) SPWM, $M = 1$, Load $= 250\ \Omega$. (b) SVPWM, $M = 1.15$, Load $= 10\ \Omega$. (c) THISPWM, $M = 1.15$, Load $= 10\ \Omega$.

shown in Fig. 1 was not used initially. A single resistor is placed directly between the neutral point of the motor and midpoint O to measure CM power capacity more conveniently. The motor is controlled using *V/f* constant mode, i.e., the ratio of modulation index to fundamental frequency (M/f_0) is kept constant. When $M = 1, f_0 = 50$ Hz.

To certify the CM power capacity in a certain modulation index, we set a series of resistor load, measure load voltage to calculate CM power and compare the maximum value. Fig. 18 shows some load voltage waveforms when CM power reaches its maximum value. Then, change modulation index from 0 to maximum to certify the load power capacity within the whole range of linear region, as shown in Fig. 19. Fig. 19 indicates that when $M<0.7$, the curves of THISPWM, SVPWM, and SPWM almost overlap, but as M continues increasing, they begin to diverge. CMV under SPWM is dominated by the switching frequency component throughout.

As modulation index increases, the rms value of CMV gradually decreases, leading to a downward trend in power capacity curve. On the other hand, for SVPWM and THISPWM,

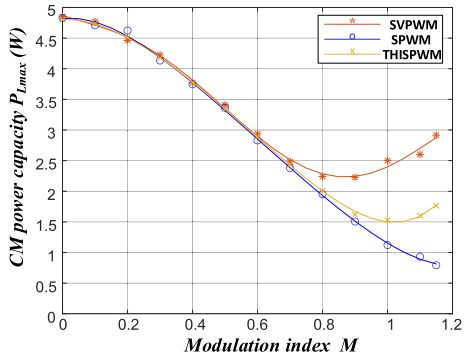

Fig. 19. CM power capacity curve of SVPWM, SPWM, and THISPWM when M varies from 0 to 1.15.

at low modulation index, the amplitude of the injected third harmonic or other zero-sequence components is relatively low, so the primary excitation in CMV is the switching frequency component, similar to SPWM. However, as modulation index increases, the low-frequency components in CMV gradually increase, resulting in enhanced power supply. Consequently, the curves undergo a turning point. Since SVPWM has a slightly higher amplitude of the third harmonic component and also includes low-frequency components such as the sixth harmonic, its power capacity curve is higher than THISPWM and the modulation index at which the turning point occurs is lower. We can also see that from Fig. 18: at high modulation index, for THISPWM and SVPWM, the main CMV component supplying power is at triple fundamental frequency (172.5 Hz) while for SPWM, it is at switching frequency (10 kHz).

B. CM Power Capacity Under DPWM0–DPWM3

At low modulation index, DPWM0–DPWM3 demonstrate strong CM power extraction capability. For example, DPWM3 provides a maximum power of up to 80 W at $M = 0.3$. However, in practical applications, CM power extraction typically does not reach such high level. For instance, encoder power consumption is usually only several watts, making measurement of tens of watts of maximum power less meaningful. More importantly, in real engineering applications, attention should be paid to the "barrel effect," focusing on the weakest link in the system. This involves considering the minimum power capacity that can be provided under full modulation index to ensure the stability of power supply.

Combining theoretical analysis with experimental observations, trends of the power curves for DPWM schemes can be generally predicted. First, as modulation index increases, the rms value of CMV decreases for the four DPWM schemes. Second, the low-frequency components that are related to strong power supply capability also gradually decreases. Considering these factors, it can be inferred that the power curves of DPWM should follow a downward trend.

Hence, two plots can be used to characterize the CM power extraction capability of DPWM0–DPWM3. The first plot shows the power curves for DPWM schemes under a constant load of

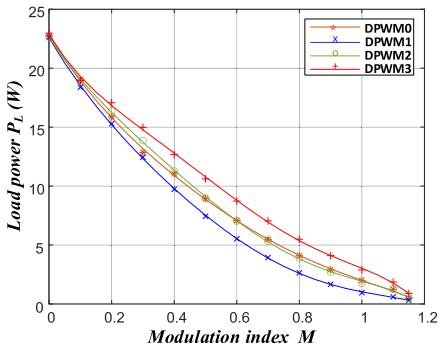

Fig. 20. Load power curve of four DPWM methods within linear modulation region when load is 150 Ω.

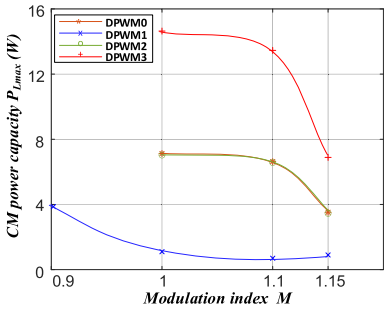

Fig. 21. CM power capacity curve of DPWM0∼DPWM3 when M>0.9.

150 Ω. Although the measured power under a constant 150 Ω load may not represent the maximum power, it provides a reasonable indication of the trend of the power curve. At high modulation index, the power obtained with a 150 Ω load may be small, making it impossible to reflect the power supply capability within the whole linear region. Therefore, it is essential to supplement measurements of the maximum power at high modulation index to characterize their power supply capability.

The CM power curves for DPWM0∼DPWM3 with a constant load of 150 Ω are shown in Fig. 20. The power curves exhibit a decreasing trend as predicted. The high-performance self-powered encoders from Posital typically consume around 2 W of power. If taking it as a benchmark, DPWM0, DPWM2, and DPWM3 are below this standard at $M = 1$, while DPWM1 is below this standard at $M = 0.9$. The CM power capacity of four DPWM methods for $M > 0.9$ are shown in Fig. 21. DPWM3 still demonstrates the highest power capability compared to the other three DPWM methods. Its minimum power capacity is approximately 6.8 W at $M = 1.15$. DPWM0 and DPWM2 are close, with minimum capacity of 3.72 W and 3.50 W, respectively. But the minimum CM power capacity of DPWM1 is not as strong as the previous three DPWM methods because due to its CMV harmonic distribution, the low-frequency component of CMV drops to a low proportion at $M = 1$, which can also be seen in Fig. 15. Fig. 22 shows the load voltage waveforms of DPWM0∼DPWM3 when CM power reaches maximum at M = 1.15. The load voltage waveforms all contain noticeable low-frequency components such as components at triple the

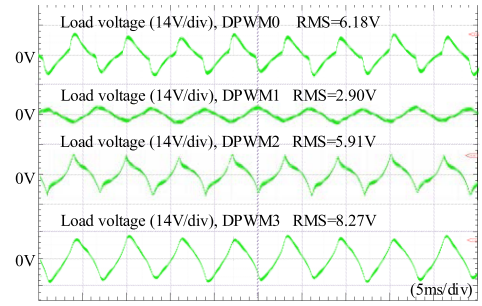

Fig. 22. Load voltage waveforms of (a) DPWM0, (b) DPWM1, (c) DPWM2, (d) DPWM3 when CM power reaches maximum at $M = 1.15$. The load is 10 Ω.

fundamental frequency. Among them, load voltage of DPWM3 exhibits the highest rms value thus it has the largest CM power.

When the modulation index M>1, as indicated previously, the dominant frequency components in DPWM0, DPWM2, and DPWM3 are the switching frequency component and the triple fundamental frequency component. Therefore, this experimental phenomenon can be explained using the multicircuit calculation method mentioned in Section II-B. For DPWM3, when $M = 1.15$, with the M/f_0 ratio kept constant, $f_0 = 57.5$ Hz.

For the switching frequency 10 kHz circuit

$$X_{fs} = 239\Omega\, R_{fs} = 70\Omega$$

$$Z_{fs} = \sqrt{X_{fs}^2 + R_{fs}^2} = 249\Omega.$$

For the triple fundamental frequency circuit

$$X_{3f_0} = 2\pi \times 3 \times 57.5 \times 7.0 \times 10^{-3}\Omega = 7.58\Omega\, R_{3f_0} = 5\Omega$$

$$Z_{3f_0} = \sqrt{X_{3f_0}^2 + R_{3f_0}^2} = 9.08\Omega.$$

When CM power reaches the maximum, experimental load resistance is 10 Ω, close to the matching impedance of 9.08 Ω for the triple fundamental frequency circuit. For the voltage amplitudes of these two frequency components, the FFT analysis results of CMV under DPWM3 at $M = 1.15$ obtained through Simulink can be approximated. The voltage amplitude of the switching frequency component is 20.36 V, while that of the triple fundamental frequency component is 19.31 V. Substituting these values into (8), i.e.,

$$P_L{}' = P_{3f_0} + P_{f_s} = \frac{\left(\frac{19.31}{\sqrt{2}}\right)^2}{\frac{9.08^2}{10} + 10 + 2 \times 5} + \frac{\left(\frac{20.36}{\sqrt{2}}\right)^2}{\frac{249^2}{10} + 10 + 2 \times 70} = 6.6\text{W}.$$

The experimentally measured power is 6.8 W, which is quite close to the calculated result obtained in this way. The abovementioned calculation method is feasible for explaining experimental phenomena and trends, but it is not recommended to replace experimental measurement. There are three main sources of error for this calculation method as follows.

TABLE II
MINIMUM POWER CAPACITY OF VARIOUS PWM TECHNIQUES

PWM techniques	Minimum power capacity	Modulation index
SPWM	1.19 W	1
THISPWM	1.53 W	1
SVPWM	2.23 W	0.8
DPWM0	3.72 W	1.15
DPWM1	0.71 W	1.1
DPWM2	3.50 W	1.15
DPWM3	6.84 W	1.15

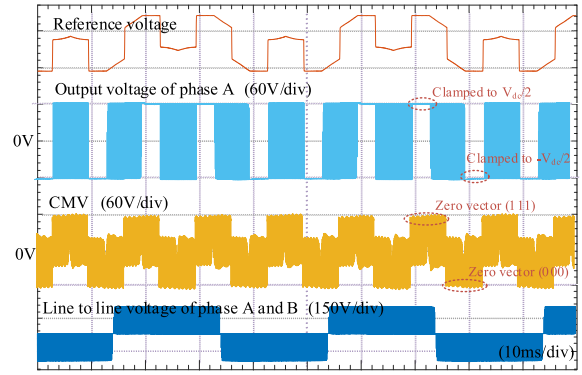

Fig. 23. Waveforms of the reference voltage and output voltage of phase A, CMV, and line voltage under DPWM3.

1) Only two main frequency components are considered. In reality, although other frequency components may have no as high amplitude as the main excitation, they still contribute some power. Especially for some components like the sixth harmonic, the circuit impedance is also relatively low.
2) Due to nonideal factors such as dead-time effect, the actual CMV waveform may not be exactly identical to the simulation. Therefore, there is difference between the Simulink FFT analysis result and the actual measurement.
3) There is some measurement error in the experimentally obtained impedance-frequency curve and reading error when using it to define the impedance at a certain frequency.

C. Comparative Analysis of Power Supply Capability Among Various Zero-Sequence Injected PWM Techniques

From an engineering perspective, it is crucial to consider the "bucket effect" – identifying the minimum limit of CM power capacity within the whole linear modulation range to ensure stable power supply. Table II summarizes the minimum power capacity and its corresponding modulation index of various PWM techniques.

It is worth noting that except for SPWM, which has a linear modulation range of 0 to 1, other zero-sequence injected PWM techniques range from 0 to 1.15. Comparatively, except for DPWM1, all other zero-sequence injected PWM techniques show an increase in CM power capacity compared to SPWM. Among them, DPWM3, with its injection of highest-amplitude zero-sequence components, demonstrates the most prominent CM power capability, reaching 6.8 W, six times that of SPWM.

D. Experimental Results for Actual Motor Operation and EMI Concern

Fig. 23 illustrates the waveforms of the reference voltage and output voltage of phase A, CMV, and line voltage under DPWM3. After zero-sequence injection, the phase output voltage is periodically clamped to the positive or negative dc bus voltage. Consequently, the two types of zero vectors (000/111) appear alternately in CMV, which leads to the generation of corresponding low-frequency components.

The CM power extraction circuit illustrated in Fig. 1 also incurs losses during power transmission, so a certain power margin should be reserved in practical applications. We measured the efficiency of the hardware circuit under different CM power conditions. The minimum efficiency was 82%. Therefore, for DPWM3, it is feasible to supply a load of 5 W. The dc–dc converter we selected outputs a dc voltage of 5 V during normal operation. It supplies a 5 Ω resistor, which corresponds to a load power of 5 W. If the load power exceeds the CM power capacity, the dc–dc converter will be unable to maintain a stable output voltage of 5 V.

We operated the motor under two typical conditions: 1) no-load at low speed and 2) heavy-load at high speed. These conditions were used to verify whether the CM power extraction circuit could work properly and to observe the impact of this scheme on the motor phase current. The experimental results are shown in Fig. 24. First, it can be seen that regardless of the motor operating condition, the dc–dc converter can work properly. Under low-speed and no-load condition, due to the small fundamental current (approximately 0.7 A), the THD of the current increases from 10.15% to 16.33%. FFT analysis reveals that the main harmonic increases are 0.01 A and 0.09 A at triple and nine times the fundamental frequency, respectively. This is because the current of the CM power extraction circuit flows through the stator windings, introducing a zero-sequence component into the phase currents. Under high-speed and heavy-load condition, the THD of the current increases from 3.72% to 4.53%. Additional small zero-sequence currents have a minor impact.

If the motor windings arrangement exhibits good sinusoidal characteristics, the zero-sequence currents will not produce significant torque ripple. In closed-loop motor control, differential-mode currents are used. So, the introduced zero-sequence currents will not significantly affect the stability of motor control. These zero-sequence currents will cause additional losses. But actually, the absolute values of the introduced harmonic currents are very small. They will not have a significant impact on the system, especially when the motor is operating under heavy load.

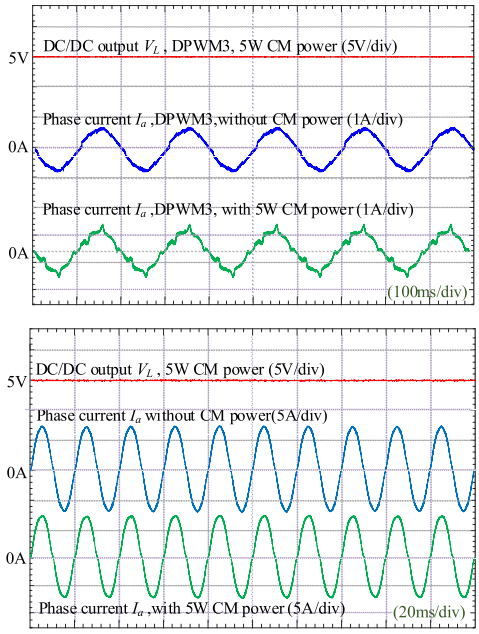

Fig. 24. Dc–dc converter output and motor phase current under DPWM3 during low-speed and no-load condition (above), high-speed and heavy-load condition (below).

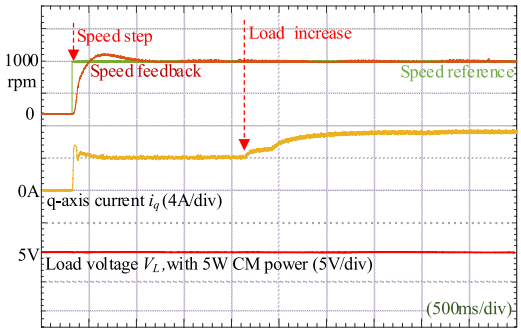

Fig. 25. Performance of the system during transient process under DPWM3.

Fig. 25 illustrates the performance of the system during transient process under DPWM3. At first, the motor operates at half-load, and its speed steps from 0 to the rated speed under experimental conditions. After the motor speed stabilizes, increase the motor load. Both the motor and the CM power extraction circuit can operate normally during transient process. The peak-to-peak value of the output voltage of the dc–dc converter is less than 1.5% during both transient and steady-state process.

Subsequently, we conducted power supply tests using proposed scheme for encoders and three-phase current sensors (with a power consumption of approximately 2 W), as shown in Fig. 26. The speed feedback from the encoder matched well with the reference speed. The output results from two identical current sensors, one powered by an auxiliary power supply and the other by common-mode voltage, were also in good agreement. This demonstrates that the proposed scheme can effectively power sensors.

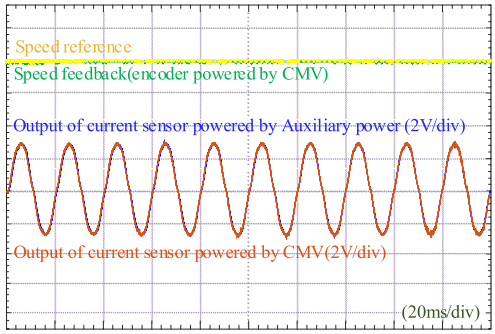

Fig. 26. Supplying power to encoders and current sensors using the CM power extraction scheme.

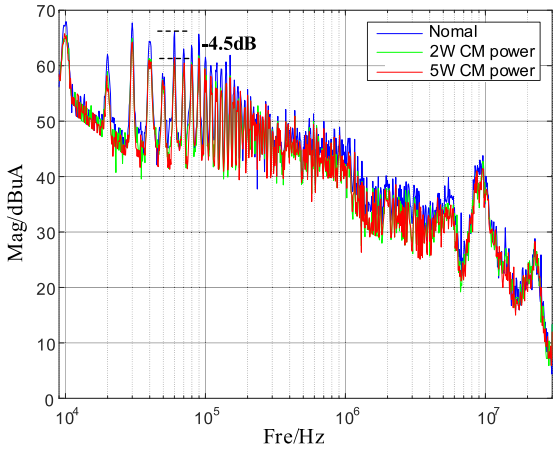

Fig. 27. Common-mode EMI test results of dc input side of the motor drive.

To assess the impact of this scheme on system EMI, we first tested the CM EMI of the dc input side of the motor drive, as shown in Fig. 27. It can be observed that after incorporating the CM power extraction circuit, multiple peaks in the CM EMI of the dc side decreased, with the maximum peak reduction being 4.5 dB. As the common-mode power extraction power increased from 2 W to 5 W, the common-mode EMI further decreased, with EMI peaks at 20 kHz and 30 kHz decreasing by about 1 dB.

As shown in Fig. 3, the system's CM EMI corresponds to the leakage current I_{cm1}, I_{cm2}, and I_{cm3}. When the CM power extraction circuit is added, a relatively large load current I_L (compared to the leakage current to GND) forms. A voltage drop is produced when I_L flows through the motor stator windings. As a result, the electric potential at point N decreases. The leakage current I_{cm3} from the motor stator to ground decreases significantly, leading to a reduction of the measured CM EMI. As the CM power increases, I_L increases and the electric potential at point N becomes lower, further reducing the CM EMI.

However, when the CM power extraction circuit is connected to the motor using short cables, it forms a loop. The high-frequency currents in cable can cause radiated EMI. We estimated the radiated EMI using the method described in [24]. The experiment results are shown in Fig. 28.

Padungtin and Tarateeraseth [24] indicated that the results of this estimation method tend to be higher compared to actual measured values. If the radiated EMI does not meet the EMC

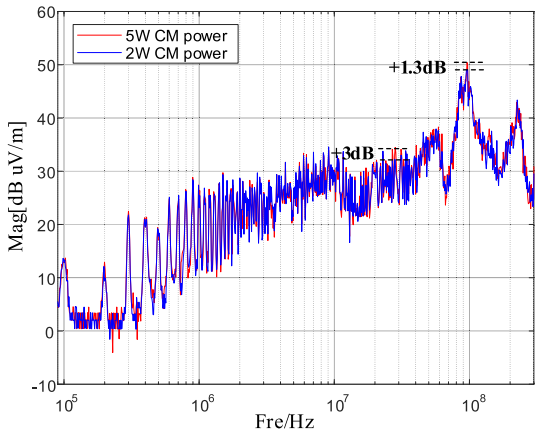

Fig. 28. Radiated EMI test results of the CM power extraction circuit.

standards, high-frequency current suppression components such as ferrite beads can be incorporated into the design of the CM power extraction PCB circuit. Since the proposed method primarily utilizes the low-frequency components of the CMV, the incorporation of components to suppress high-frequency currents will not significantly affect the power extraction. Additionally, integrating the common-mode power extraction PCB circuit with the motor winding neutral point can also reduce the length of the cable used.

V. Conclusion

The main innovation of this article is the theory of CM power transfer and the exploration of zero-sequence injection methods to improve the power capacity of CM power extraction. The conclusions of this article are as follows.

1) The calculation method for CM power is presented based on the power superposition theory. CMV is a voltage source composed of multiple frequencies so theoretical analysis of total power supply in CM circuits can be conducted using Fourier decomposition. Due to skin effect, the equivalent impedance of CM power supply circuits is much smaller at low frequency. Therefore, low-frequency components of CMV have greater potential for CM power supply.
2) The impact of zero-sequence injection during PWM on the characteristics of CMV is studied. Injecting zero-sequence components such as triple fundamental frequency into modulation wave can generate corresponding low-frequency components in CMV and their amplitudes are proportional to the zero-sequence injection amount. All PWM methods based on NTV principle have the same rms value of CMV. Therefore, injecting high-amplitude zero-sequence components can effectively increase the proportion of low-frequency components in CMV and improve CM power supply.
3) A modulation method DPWM3 that is the most advantageous for enhancing the CM power supply has been identified. Both theoretical analysis and experiments demonstrate that compared to SPWM with no zero-sequence injection, CM power capacity has been increased by more than five times when DPWM3 is adopted.

This method of improving CM power supply from PWM does not require additional circuit hardware. Moreover, since it primarily utilizes low-frequency components in CMV for power supply, it imposes low requirements on the switching frequency of the inverter, making it more flexible for practical applications.

Currently, the design of the CM power extraction circuit is primarily based on commercially mature integrated modules for validating the feasibility of this solution. Addressing how this circuit can adapt to harsher conditions and further reduce losses during energy transmission are issues worthy of continued research and optimization in the future for better engineering practicality.

References

[1] G. L. Skibinski, R. J. Kerkman, and D. Schlegel, "EMI emissions of modern PWM AC drives," *IEEE Ind. Appl. Mag.*, vol. 5, no. 6, pp. 47–80, Nov./Dec. 1999.
[2] J. Kalaiselvi and S. Srinivas, "Bearing currents and shaft voltage reduction in dual-inverter-fed open-end winding induction motor with reduced CMV PWM methods," *IEEE Trans. Ind. Electron.*, vol. 62, no. 1, pp. 144–152, Jan. 2015.
[3] Y. Zhang, Q. Li, and D. Jiang, "A motor CM impedance based transformerless active EMI filter for DC-side common-mode EMI suppression in motor drive system," *IEEE Trans. Power Electron.*, vol. 35, no. 10, pp. 10238–10248, Oct. 2020.
[4] L. Xing and J. Sun, "Conducted common-mode EMI reduction by impedance balancing," *IEEE Trans. Power Electron.*, vol. 27, no. 3, pp. 1084–1089, Mar. 2012.
[5] L. Yang, H. Zhao, S. Wang, and Y. Zhi, "Common-mode EMI noise analysis and reduction for AC–DC–AC systems with paralleled power modules," *IEEE Trans. Power Electron.*, vol. 35, no. 7, pp. 6989–7000, Jul. 2020.
[6] S. Ogasawara, H. Ayano, and H. Akagi, "An active circuit for cancellation of common-mode voltage generated by a PWM inverter," *IEEE Trans. Power Electron.*, vol. 13, no. 5, pp. 835–841, Sep. 1998.
[7] S. Ohara, S. Ogasawara, T. Masatsugu, K. Orikawa, and Y. Yamamoto, "A novel active common-noise canceler combining feedforward and feedback control," in *Proc. IEEE Energy Convers. Congr. Expo.*, Cincinnati, OH, USA, 2017, pp. 2469–2475.
[8] Z. Shen, D. Jiang, Z. Liu, D. Ye, and J. Li, "Common-mode voltage elimination for dual two-level inverter-fed asymmetrical six-phase PMSM," *IEEE Trans. Power Electron.*, vol. 35, no. 4, pp. 3828–3840, Apr. 2020.
[9] A. L. Julian Oriti and T. A. Lipo, "A new space vector modulation strategy for common mode voltage reduction [in PWM invertors]," in *Proc. 28th Annu. IEEE Power Electron. Specialists Conf., Formerly Power Conditioning Specialists Conf. 1970/71. Power Process. Electron. Specialists Conf. 1972*, St. Louis, MO, USA, 1997, vol. 2, pp. 1541–1546.
[10] E. Un and A. M. Hava, "A near state PWM method with reduced switching frequency and reduced common mode voltage for three-phase voltage source inverters," in *Proc. IEEE Int. Electric Machines Drives Conf.*, Antalya, Turkey, 2007, pp. 235–240.
[11] Z. Liu, Z. Zheng, S. D. Sudhoff, C. Gu, and Y. Li, "Reduction of common-mode voltage in multiphase two-level inverters using SPWM with phase-shifted carriers," *IEEE Trans. Power Electron.*, vol. 31, no. 9, pp. 6631–6645, Sep. 2016.
[12] L. Fan, Z. Liu, and D. Jiang, "An integrated power supply design for motor encoder utilizing common-mode voltage with phase shifted SPWM," in *Proc. IEEE 4th Int. Elect. Energy Conf.*, Wuhan, China, 2021, pp. 1–5.
[13] S. Saggini, F. Ongaro, L. Corradini, and A. Affanni, "Low-Power energy harvesting solutions for wiegand transducers," *IEEE J. Emerg. Sel. Topics Power Electron.*, vol. 3, no. 3, pp. 766–779, Sep. 2015.
[14] Y. Takemura, N. Fujinaga, A. Takebuchi, and T. Yamada, "Batteryless hall sensor operated by energy harvesting from a single wiegand pulse," *IEEE Trans. Magn.*, vol. 53, no. 11, Nov. 2017, Art. no. 4002706.
[15] M. Taghavi, A. Sadeghi, A. Mondini, B. Mazzolai, L. Beccai, and V. Mattoli, "Triboelectric smart machine elements and self-powered encoder," *Nano Energy*, vol. 13, pp. 92–102, 2015.

[16] L. Fan et al., "Analysis and utilization of common-mode voltage in inverters for power supply," *IEEE Trans. Power Electron.*, vol. 38, no. 7, pp. 8811–8824, Jul. 2023.

[17] D. H. Park, M. Kim, and W. J. Lee, "Three-phase and single-phase motor drive system with single three-phase two-level inverter for independent speed control," *J. Power Electron.*, vol. 22, pp. 40–49, 2022.

[18] H. L. Lewis-Rzeszutek, R. M. Tallam, R. Phukan, M. Solveson, and T. Clancy, "Simulation of cable charging current and its effects on operation of low power AC drives," in *Proc. IEEE Energy Convers. Congr. Expo.*, Milwaukee, WI, USA, 2016, pp. 1–7.

[19] R. M. Tallam and D. Leggate, "Control of PWM voltage source inverter in the pulse dropping region to reduce reflected wave motor over-voltage," in *Proc. IEEE Energy Convers. Congr. Expo.*, Phoenix, AZ, USA, 2011, pp. 3900–3905.

[20] B. Mirafzal, G. L. Skibinski, R. M. Tallam, D. W. Schlegel, and R. A. Lukaszewski, "Universal induction motor model with low-to-high frequency-response characteristics," *IEEE Trans. Ind. Appl.*, vol. 43, no. 5, pp. 1233–1246, Sep./Oct. 2007.

[21] D. Grahame Holmes and T. A. Lipo, "Modulation of one inverter phase leg," in *Proc. Pulsewidth Modulation Power Converters, Princ. Pract.*, 2003, pp. 95–153.

[22] P. A. Dahono, Y. Sato, and T. Kataoka, "Analysis and minimization of harmonics in the AC and DC sides of PWM inverters," *IEEJ Trans. Ind. Appl.*, vol. 115, no. 5, pp. 553–561, Spr. 1995.

[23] K. Zhou and D. Wang, "Relationship between space-vector modulation and three-phase carrier-based PWM: A comprehensive analysis [three-phase inverters]," *IEEE Trans. Ind. Electron.*, vol. 49, no. 1, pp. 186–196, Feb. 2002.

[24] W. Padungtin and V. Tarateeraseth, "Comparison of radiated EMI prediction methods from measured common-mode currents," in *Proc. 25th Int. Conf. Elect. Machines Syst.*, Chiang Mai, Thailand, 2022, pp. 1–4.